



Exploring rift geodynamics in Ethiopia through olivine-spinel Al-exchange thermometry and rare-earth element distributions

Kevin Wong^{a,*}, David Ferguson^a, Simon Matthews^b, Daniel Morgan^a, Amdemichael Zafu Tadesse^c, Yared Sinetebeb^d, Gezahegn Yirgu^e

^a School of Earth and Environment, University of Leeds, Leeds, LS2 9JT, UK

^b Institute of Earth Sciences, University of Iceland, Sturlugata 7, 102 Reykjavik, Iceland

^c Department of Geosciences, Environment, and Society, Université Libre de Bruxelles, Brussels, Belgium

^d Ethiopian Electric Power, P.O. Box 15881, Addis Ababa, Ethiopia

^e School of Earth Sciences, Addis Ababa University, P.O. Box 1176, Addis Ababa, Ethiopia

ARTICLE INFO

Article history:

Received 22 October 2021

Received in revised form 22 July 2022

Accepted 13 September 2022

Available online 23 September 2022

Editor: R. Hickey-Vargas

Keywords:

continental rifting

melt generation

melt chemistry

East African Rift

melt thermometry

ABSTRACT

Understanding the process of continental break-up requires knowledge of the geodynamics of mature rift systems close to the point of plate rupture. In Ethiopia, late-stage continental rifting occurs in a magma-rich setting where extensional processes correlate closely with magmatic and volcanic activity. Unravelling the role that mantle and lithospheric dynamics play in sustaining rifting in Ethiopia is key to improving models of late-stage continental rift evolution. In this study we provide petrological constraints on the physical characteristics of magma production using volcanic samples from the northern Main Ethiopian Rift (MER) and central Afar. Olivine crystallisation temperatures provide information about the thermal state of mantle-derived magmas generated by the mantle during upwelling and melting. These temperatures, determined by Al-exchange thermometry, are used in conjunction with other geochemical and geophysical constraints in inversion models of melting a multi-lithology mantle to find the best-fitting geodynamic parameters that can reproduce observed magma compositions and melt volumes. Our model results suggest that the potential temperature of the Ethiopian mantle is hotter than ambient mantle by $\geq 150^\circ\text{C}$, and is elevated to a similar degree across the MER and Afar. We predict significant variations in lithospheric thickness between the MER (90 km) and Afar (50–70 km), with Afar also likely to have a higher portion of fusible mantle domains. This thinner lithosphere and/or more productive mantle is required to generate the larger volumes of magma inferred to have been intruded into the Afar crust. The geodynamic differences between these two settings can be attributed to the more-evolved state of the Afar rift and its proximity to the centre of the Afar plume.

© 2022 The Author(s). Published by Elsevier B.V. This is an open access article under the CC BY license (<http://creativecommons.org/licenses/by/4.0/>).

1. Introduction

The influence of mantle dynamics on late-stage continental rifting and the formation of ocean basins is a subject of ongoing research and debate (e.g., Rychert et al., 2012; Ferguson et al., 2013b; Armitage et al., 2015; Gallacher et al., 2016). The presence of upwelling thermo-chemical plumes beneath magmatically active rifts influences the temperature, composition, and lithology of the sub-rift mantle, governing the conditions of magma generation. As late-stage extension in volcanic rifts is believed to be strongly affected by repeated intrusions of magma that both accommodate extension and alter the thermo-mechanical structure of the crust

(e.g., Bastow and Keir, 2011), unravelling the role that mantle conditions play in continental rift magmatism is key to understanding the geodynamic context of mature rifts.

Ongoing rift-related volcanism in East Africa provides an opportunity to study the intertwining of continental rift processes with mantle plume behaviour. Flood basalts in northern Ethiopia are correlated with the impingement of a mantle plume head at the base of the Ethiopian lithosphere at ~ 30 Ma (e.g., Hofmann et al., 1997) and a persistent plume influence to the present day is inferred from both magma chemistry (e.g., Rooney et al., 2012a; Ferguson et al., 2013b) and geophysical observations (e.g., Bastow et al., 2008). These studies highlight a significant thermal and geochemical deviation of the present-day Ethiopian mantle from the ambient mid-ocean ridge basalt (MORB) mantle source. Thermochemical anomalies will affect mantle melting behaviour, enhanc-

* Corresponding author.

E-mail address: eekw@leeds.ac.uk (K. Wong).

ing melt production due to elevated mantle temperatures and the presence of more fusible lithologies.

One regularly explored avenue of resolving sub-rift mantle characteristics has been to determine mantle potential temperatures (T_p). Petrological methods estimating Ethiopian mantle temperature strongly suggest an excess T_p of $> 100^\circ\text{C}$ above the ambient MORB mantle value of $\sim 1350^\circ\text{C}$ (e.g., Rooney et al., 2012b). Basalt major element thermometry returns T_p values of $1400\text{--}1490^\circ\text{C}$ for the Main Ethiopian Rift (MER) and Afar (Rooney et al., 2012b), in close concordance with trace element models for Afar basalts which suggest melting at a similar T_p beneath a relatively thick lithosphere (Ferguson et al., 2013b; Armitage et al., 2015). However, a caveat of using methods based solely on basalt geochemistry is that assumptions must be made about mantle source composition, which will affect the thermodynamic properties of the mantle and hence the composition of generated melts (see appendix of Matthews et al., 2021). Furthermore, geochemical equilibrium between the mantle and observed melts must be established or assumed.

Geophysical approaches have also been used to infer the melting behaviour of the Ethiopian mantle, but cannot straightforwardly resolve the thickness of the lithosphere. For example, S-to-P receiver functions highlight the absence of a seismically distinct lithosphere-asthenosphere boundary (LAB) beneath the MER and Afar rift axes (Rychert et al., 2012; Lavayssi re et al., 2018) demonstrating that melt within the lithosphere may obscure a prominent LAB from seismic imaging (Lavayssi re et al., 2018). Numerical models that reconcile both magma chemistry and receiver function observations argue for an elevated T_p of 1450°C beneath a significantly thinned, yet still present ($\sim 50\text{ km}$ thick) mantle lithosphere (Armitage et al., 2015). Similar observations from Rayleigh wave tomography agree that sub-rift mantle melting is likely to be relatively deep, and driven by active melt-retention buoyancy (Gallacher et al., 2016).

In addition to raising mantle temperatures, plumes can also affect sub-rift melting processes by altering the lithological composition of the mantle. The extension of sub-rift seismic anomalies to the lower mantle beneath Ethiopia (e.g., Bastow et al., 2008) and highly radiogenic isotopes from MER and Afar basalts (e.g., Rooney et al., 2012a) suggest that the plume is compositionally distinct from ambient mantle. An important feature in this regard is the possible presence of more fusible pyroxenitic domains derived from the recycling of oceanic crust (e.g., Herzberg, 2011; Shorttle et al., 2014) or through the dripping of pyroxenitic material from thermally and gravitationally unstable metasomatised lithosphere (Furman et al., 2016). Indeed the presence of asthenospheric mantle pyroxenites have previously been posited as a possible driver for deep melting beneath Ethiopia in the absence of significantly elevated T_p (Rooney et al., 2012b). Additionally, it is also probable that the Ethiopian mantle, like many other plume-affected localities, is partially composed of refractory harzburgitic material, the depleted residue from previous melting (Stracke et al., 2019). The presence of multiple melting and non-melting lithologies in the Ethiopian mantle will dictate the thermal pathway taken during decompression and melting, which will likely deviate from that inferred via single-lithology (peridotite) melting models (Phipps Morgan, 2001; Matthews et al., 2021). Furthermore, melting a mixed lithology mantle will produce magmas that differ in major element, trace element, and radiogenic isotopic compositions compared to those derived from a purely peridotite source (Herzberg, 2011; Shorttle et al., 2014). The recent study of Ethiopian mantle xenoliths has additionally highlighted the presence of highly fusible metasomatic domains in the Ethiopian lithospheric mantle which may also contribute to the chemistry of erupted rift basalts (e.g., Casagli et al., 2017; Rooney et al., 2017). Petrological models linking the observed composition of rift basalts to the composition

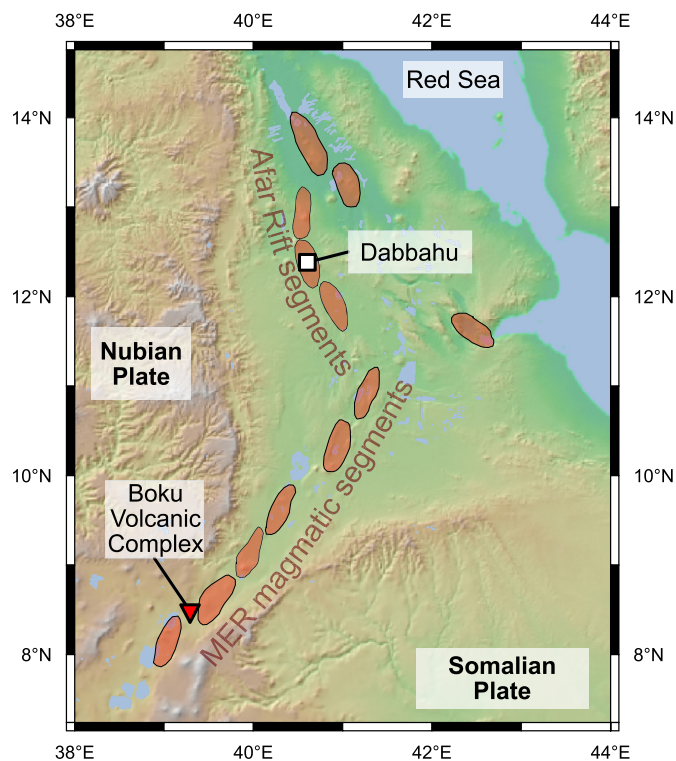


Fig. 1. Map of the northernmost East African Rift showing the sampled locations in our study, with Main Ethiopian Rift (MER) and Afar Rift magmatic segments highlighted in red (after Hayward and Ebinger, 1996). (For interpretation of the colours in the figure(s), the reader is referred to the web version of this article.)

and thermal state of a multi-lithology mantle source are therefore necessary to explore how multiple melting lithologies in the sub-rift mantle may contribute towards magmatism and rifting in Ethiopia.

In this study we investigate melt generation beneath the MER and Afar via a mantle melting model constrained by olivine crystallisation temperatures and REE concentrations observed in rift zone magmas. Our multi-lithology melting approach is based on that of Matthews et al. (2021) who demonstrated that variations in olivine crystallisation temperatures can be related to the temperature and lithological composition of the melting mantle and can therefore be used to estimate mantle T_p independent of magma chemistry. This method provides an alternative and complementary approach to previous studies that investigated mantle temperatures in Ethiopia using peridotite-only melting models (e.g., Rooney et al., 2012b; Ferguson et al., 2013b; Armitage et al., 2015).

2. Samples and methods

The olivine crystals analysed in this study were separated from olivine-phyric basaltic scoria collected from monogenetic cones in the MER and Afar related to late-stage magmatic-tectonic rift zones (e.g., Rooney et al., 2011). Samples from the MER were collected from a cone (8.490 N, 39.294 E) within the Boku Volcanic Complex; (e.g., Tadesse et al., 2019, see Fig. 1). The main phenocryst phase within this scoria is olivine with plagioclase feldspar also present as a smaller fraction ($< 15\%$) phenocryst phase. Samples from Afar were collected at the recently active Dabbahu Rift Zone and are predominantly olivine-phyric (e.g., Ferguson et al., 2010, see Fig. 1). Picked olivines were mounted in epoxy resin and polished for electron probe microanalysis (EPMA).

Extension within the MER at Boku is primarily accommodated by a segmented network of magma-induced faults in the rift centre, along which scoria cones are found (e.g., Rooney et al., 2011).

Seismic evidence suggests that the lower crust in this section of the MER has been modified by repeated dyke intrusions (e.g., Maguire et al., 2006; Hammond et al., 2011). At Boku, scoria cones are associated with post-caldera basaltic activity dating to ~200 ka (Tadesse et al., 2019). In Afar, the tectonic-magmatic segmentation of the rift system is more distinct, and faulting and volcanism are strongly focused along magmatic rift zones (Hayward and Ebinger, 1996). The crust here is thinner compared to the MER and predominantly igneous in nature (Hammond et al., 2011). At the Dabbahu rift segment, which has been the locus of magmatically driven extension in this section of the rift system since at least ~200 ka (Ferguson et al., 2013a), the most recent volcanic activity occurred in 2005–2010 and involved a series of intrusive and eruptive events (e.g., Ferguson et al., 2010).

2.1. Olivine-spinel Al-exchange thermometry

Olivine and spinel are among the first phases to crystallise from mantle-derived melts, and for co-crystallisation to occur they must be on the liquidus together. Spinel inclusions entrapped within olivine phenocrysts can therefore record the initial chemical conditions under which mantle-derived magmas begin olivine-spinel co-crystallisation. The compatibility of Al in olivine is a strong function of temperature, and unlike the Fe-Mg system, Al is slow-diffusing and therefore less susceptible to post-crystallisation resetting (Spandler and O'Neill, 2010). The olivine-spinel Al-exchange thermometer can hence provide a means of estimating olivine crystallisation temperatures (T_{crys}) for magmas without requiring knowledge of the initial melt composition (Coogan et al., 2014).

Experiments on Al partitioning between olivine and spinel demonstrate that partitioning is not significantly influenced by pressure, silica activity, or oxygen fugacity, but instead is strongly correlated with temperature (Wan et al., 2008; Coogan et al., 2014). However, the partitioning of P into olivine and Ti into spinel may affect Al uptake and must also be considered (as noted by Coogan et al., 2014; Jennings et al., 2019).

This thermometer has previously been used to investigate olivine T_{crys} at mid-ocean ridges (Coogan et al., 2014; Matthews et al., 2021) and plume settings (e.g., Coogan et al., 2014; Heinonen et al., 2015; Jennings et al., 2019; Matthews et al., 2021), but has not been previously applied to continental rift magmas. Primary T_{crys} , liquidus temperatures of the most primitive mantle-derived melts, obtained for non-rift tectonic settings, either directly or through secondary correction of Al-exchange T_{crys} values, show substantial variations between MORB and plume-derived basalts, consistent with elevated mantle T_p at plume settings. However, without further constraints on melting geometry and mantle source composition, differences in T_p cannot be resolved from differences in T_{crys} alone (Matthews et al., 2021). In this study we therefore integrate results from olivine-spinel Al-exchange thermometry with other constraints on magmatic processes in the MER and Afar to constrain likely values for mantle T_p .

2.2. Analytical methods

Geochemical data on olivine and spinel were collected by EPMA over three analytical sessions using the JEOL JXA8230 microprobe at the University of Leeds, U.K. Only olivines completely enclosing spinel inclusions were selected. Beam conditions and detection limits are listed in the Supplementary Materials.

During the first session, qualitative maps were recorded for the areas surrounding and including the spinel inclusion to assess the presence of zoning in Al, P, Ni, Ca and Mg within both the host olivine and spinel inclusion, following the method and analytical conditions of Matthews et al. (2021) (see Supplementary Materials

and Dataset S1). These maps illustrate that the majority of crystals do not show any significant variability in Al and P count rates on the scale of the map (~100 μm), suggesting that Al uptake in olivine resulting from increased P concentrations is minimal (Coogan et al., 2014) and equilibrium Al was not changing during crystallisation. Zoning in Mg, Ni, and Ca is observed and these zones were avoided if possible during subsequent point analyses.

In the following two sessions, quantitative analyses within both phases were performed for Fe, Mg, Si, Mn, Al, Ca, Cr, Ni, Ti, and P using the qualitative maps as guidance. Longer count times were taken for Al in olivine, as it is present in low concentrations (< 700 ppm, Coogan et al., 2014). Points within olivine were selected at least 10 μm away from the olivine-spinel boundary to avoid secondary fluorescence of X-rays from spinel into olivine which increases the measured Al_2O_3 in olivine (Jennings et al., 2019). Care was also taken to avoid selecting points across zones of Fe-Mg evident from qualitative maps. Analytical conditions for quantitative point analyses in olivine and spinel are provided in Supplementary Tables S1 and S2 respectively. Secondary standard analyses are included in Supplementary Dataset S2.

Uncertainties in olivine crystallisation temperature are determined through Monte Carlo propagation ($n = 10000$) including an inherent minimum experimental uncertainty of 14 °C to account for the combined uncertainty of the thermometer calibration (Matthews et al., 2016).

2.3. Mantle melting forward model

Predicting observable properties such as olivine T_{crys} , basalt REE compositions, and melt fractions from mantle T_p necessitates several key assumptions concerning the mechanics of melt segregation, accumulation, and mantle source composition. A model of mantle melting allows us to determine these parameters by predicting thermal pathways from melt generation to crystallisation as a function of mantle T_p and lithological composition.

Decompressing solid mantle of multiple lithologies initially follows a mantle adiabat dependent on mantle T_p and composition. Upon crossing the solidus of one of the components, melting commences and heat is converted into latent heat of fusion, resulting in a decrease to the mantle adiabatic gradient. We use pyMelt, a Python 3 module which calculates the thermodynamic behaviour of a multi-component mantle during adiabatic decompression (Matthews et al., 2021, 2022), following established expressions for multi-lithology melting (Phipps Morgan, 2001). In pyMelt, the mantle adiabat is calculated during decompression melting assuming that melt and residue remain in thermal equilibrium. Melting ceases at the LAB, after which the melts follow a basalt adiabat to crustal pressures where olivine crystallisation begins. We assume that the melt is not cooled as it passes through the lithosphere, and strictly follows the basalt adiabat, which is appropriate when melt fluxes are high and heat advection dominates over conduction. The input parameters for our forward model are those that control the thermal pathway of the melting mantle and therefore melt fraction and by extension melt thickness: T_p , mantle composition, lithospheric thickness, and crystallisation pressure. We select a tri-lithology mantle comprising non-melting harzburgite (after Shorttle et al., 2014), a pyroxenite component melting like KG1 (Kogiso et al., 1998), and a lherzolite melting like KLB-1 (Takahashi, 1986). These lithologies in particular are selected for continuity with Matthews et al. (2021). Although our modelling approach necessitates choosing particular lithologies, the inclusion of pyroxenite can equivalently be interpreted as the bulk mantle being made more fusible (e.g., through refertilisation of a lherzolite), and likewise harzburgite interpreted as the bulk mantle becoming more refractory. To provide additional constraints on melt production the pyMelt code has been modified in this study to

include calculations of the concentrations of incompatible trace elements in the melt following McKenzie and O'Nions (1991) (see Supplementary Materials).

2.4. Inverse model

The pyMelt forward model allows us to predict T_{crys} , trace element composition, and melt thickness from a given T_p , mantle composition, lithospheric thickness and crystallisation pressure, assuming that the first olivine crystallises at or near the primary basalt liquidus temperature. Through inversion of this forward model we can use observed T_{crys} , rare-earth element (REE) distributions, and thickness of igneous crust to reconstruct the thermal pathway undertaken by mantle melts and obtain T_p , mantle lithological composition, and the uncertainty in these parameters while accounting for uncertainty in the observed data. Inverse modelling is performed using the Python 3 wrapper of MULTINEST, a Bayesian inference tool which utilises a Monte Carlo Markov Chain nested sampling algorithm (Buchner et al., 2014; Feroz et al., 2019, and references therein). A significant number of forward models (~20,000-30,000) are run with values selected for each parameter according to prior distributions we define based on the parameter uncertainty (e.g., LAB depth) or left open for unconstrained parameters (e.g., T_p). The result of each forward model is subsequently compared to observed T_{crys} , La/Yb and Dy/Yb ratios, and igneous crustal thickness. Model likelihood, a measure of the misfit of the model to the data, is calculated and the model parameters are refined until sufficient solutions of highest likelihood are available such that the posterior probability distributions for each parameter can be estimated (~ 8,000-10,000 forward model solutions to the inverse problem). Although the inversion will favour solutions falling near the medians of the parameter prior estimates, high-likelihood solutions towards the limits of these ranges are also accepted.

2.4.1. Prior distributions for Moho and LAB depth

Before inversion we establish estimates and uncertainties for lithospheric thickness and crystallisation pressure to use as prior distributions. The depth of the LAB controls where melting ceases and previous petrological models have argued that significant shallow mantle melting does not occur beneath Ethiopia (Rooney et al., 2011; Ferguson et al., 2013b; Armitage et al., 2015). This is because erupted melts have elevated medium REE to heavy REE ratios (e.g., Dy/Yb), consistent with melt production in the presence of the mineral garnet, which is only stable in lherzolite at depths ≥ 85 km. The retention of this garnet-field melting signature suggests that low pressure melting is likely impeded by the presence of a > 50 km thick lithospheric lid (e.g., Armitage et al., 2015). These petrological inferences on melting depths are generally consistent with Rayleigh wave tomography, which highlights a low shear velocity region of melt generation at > 75 km (Gallacher et al., 2016). Given these observations we would expect a LAB depth of 60 ± 20 km for both the MER and Afar, which we can use as prior distributions (Table 1).

Crystallisation is likely to commence at the base of the crust where ascending melts initially pool (Rooney et al., 2005; Dessisa et al., 2013) before continuing to lower pressures via crustal plumbing systems (< 0.5 GPa; Rooney et al., 2005; Field et al., 2013; Iddon and Edmonds, 2020). Although some crystallisation is expected to occur at lithospheric mantle pressures (e.g., Rooney et al., 2005), the base of the crust provides a reasonable estimate for the earliest onset of crystallisation. Ethiopian crustal thickness is well characterised though seismic imaging (e.g., Maguire et al., 2006; Hammond et al., 2011; Lavayssière et al., 2018) and recent MER and Afar crustal thickness estimates of 28 ± 3 km and 23 ± 2

Table 1

Table summarising prior distributions and data constraints on our inversions. References as follows: 1. Ferguson et al. (2013b), 2. Armitage et al. (2015), 3. Lavayssière et al. (2018), 4. McDonough and Sun (1995), 5. Workman and Hart (2005), 6. Gale et al. (2013), 7. Tadesse et al. (2019). The composition KG1 refers to 50:50 DMM:average MORB.

Prior distributions	Boku Volcanic Complex	Dabbahu Rift	References
LAB depth (km)	60 ± 20	60 ± 20	1, 2
Moho depth (km)	28 ± 3	23 ± 2	3
Lherzolite	PM $\pm 10\%$	PM $\pm 10\%$	4
Pyroxenite	KG1 $\pm 10\%$	KG1 $\pm 10\%$	5, 6
Data constraints			
$T_{crys}^{primary}$ ($^{\circ}$ C)	1426 ± 26	variable (see text)	This study
t_m (km)	4.5 ± 1.5	13 ± 2	This study; 2
La/Yb	9.70 ± 0.85	2.17 ± 0.07	1, 7
Dy/Yb	7.34 ± 1.93	2.21 ± 0.13	1, 7

km respectively are used as prior distributions for our inversions (Table 1).

2.4.2. Melting geometry constraints and igneous thickness

The geometry of the melting region influences both the composition and total quantity of melts produced during mantle upwelling (e.g., Plank and Langmuir, 1992). Melting of the asthenospheric mantle beneath Ethiopia during rifting may be driven by passive decompression beneath a thinning lithosphere, similar but not identical to a mid-ocean ridge environment. While the triangular geometry that arises from passively driven upwelling probably does not capture the true complexity of sub-rift melting, it provides a means to test how changing mantle temperature and lithospheric thickness affects melt production (see Supplementary Materials for an assessment of the impact of active mantle upwelling). Owing to the large scale of the seismic velocity anomaly in the sub-rift mantle (Hammond et al., 2013) we believe that modelling melting with an alternative plume conduit geometry is inappropriate. We also require that the melting mantle must be buoyant with respect to ambient mantle otherwise mantle upwelling will not be possible (e.g., Shorttle et al., 2014), which effectively limits the proportion of pyroxenite in the permitted solutions.

Total crustal thickness in the MER and southern Afar appears to be largely maintained until the final stages of continental rifting by magmatic intrusion (Bastow and Keir, 2011). Seismic studies of the rift-axis crust illustrate that the thickness of the upper crust is predominantly affected by rift-related thinning while the lower crust remains thick owing to intrusion (Maguire et al., 2006; Hammond et al., 2011). By comparing pre- and post-rift upper and lower crust at Dabbahu, Armitage et al. (2015) inferred that the Afar crust comprises 11-15 km of magmatic material. Adopting their method, we can estimate the thickness of melt (t_m) in the MER. To do this we use thicknesses of original, unstretched crust inferred from the Ethiopian plateau of 21 km for the upper crust and 23 km for the lower crust (Maguire et al., 2006) and upper and lower crustal thicknesses within the MER near Boku that range from 14-17 and 16-20 km respectively (Maguire et al., 2006). This gives a stretch factor of 1.2-1.5 and suggests that the lower crust comprises 3-6 km of igneous material. We therefore choose t_m of 4.5 ± 1.5 km and 13 ± 2 km for the MER and Afar respectively (Table 1).

2.4.3. Rare-earth element ratio constraints

Our inversions can be further constrained by comparing REE concentrations from pyMelt to those observed in the Boku and Dabbahu basalts (Table 1). The La/Yb and Dy/Yb ratios of the lavas are matched to those generated by our model. We use ratios as they are less affected by crystal fractionation and accumulation than absolute concentrations.

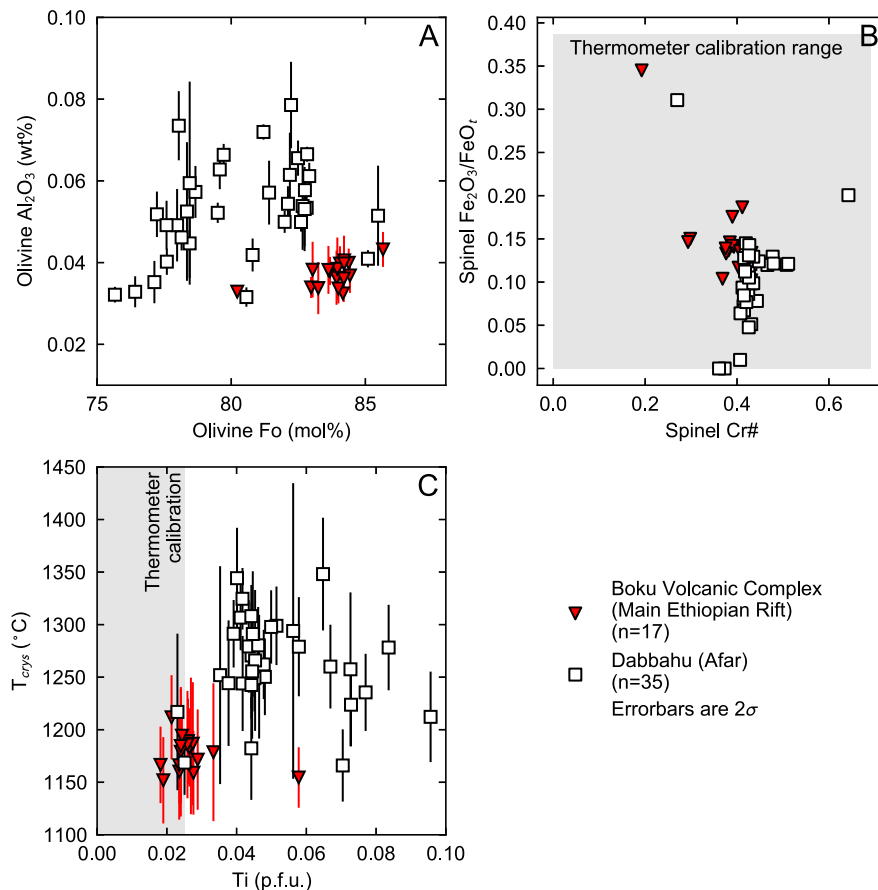


Fig. 2. A. Al_2O_3 concentration in olivine as a function of their Fo content for all Ethiopian Rift and Afar samples. Uncertainties of Al_2O_3 are presented as 2σ error bars; uncertainties in Fo are smaller than the marker size. B. Cr_2O_3 concentration in spinel as a function of estimated $\text{Fe}_2\text{O}_3/\text{FeO}_t$ content for all Ethiopian Rift and Afar samples. $\text{Fe}_2\text{O}_3/\text{FeO}_t$ is estimated using the stoichiometric method of Droop (1987). The shaded area shows the calibrated range of the olivine-spinel Al exchange thermometer. C. Olivine crystallisation temperature as a function of Ti (per formula unit in spinel). Temperature uncertainties are presented as 2σ as determined from Monte Carlo error propagation. The shaded area shows the Ti calibration range of the thermometer (Wan et al., 2008; Coogan et al., 2014).

REE compositions must be established for the two melting lithologies in our model. The prior distributions for the lherzolite REE concentrations are defined as normal distributions centred on the concentrations of La, Dy, and Yb in the primitive mantle (PM; McDonough and Sun, 1995), with a standard deviation of 10% of their concentration as reported. We additionally consider the consequences of using lower concentrations for lherzolite more typical of the depleted mantle (DMM), which are found to yield similar results to PM-composition lherzolite (Supplementary Materials). A 50:50 mixture of DMM (Workman and Hart, 2005) and average MORB (Gale et al., 2013) is used to approximate the REE composition of a KG1-like mixed-lithology pyroxenite. Like our lherzolite we allow KG1-composition pyroxenite to vary according to a normal distribution with a standard deviation of 10% centred on the reported La, Dy, and Yb concentration. Post-inversion, we also allow for the possible addition of small-fraction melts from destabilisation of metasomatised domains in the Ethiopian lithospheric mantle (e.g., Casagli et al., 2017; Rooney et al., 2017), which can occur as ascending melts interact with the lithosphere (e.g., Rooney et al., 2017) or via lithospheric drip (Furman et al., 2016). We calculate the composition of a small-fraction (~1%) batch melt generated from a source based on xenolith compositions representative of the sub-Ethiopian lithospheric mantle (Casagli et al., 2017, see also Supplementary Materials) and assess whether the addition of small volumes of this melt improves the fit to the observed REE ratios. Finally, we modify the absolute concentrations of REEs in the final basalt to account for fractional crystallisation of olivine in the lithosphere.

3. Results

3.1. Olivine and spinel chemistry

Mean olivine and spinel compositions determined by repeat analyses are shown in Fig. 2. The complete dataset is presented as Supplementary Dataset S2.

Boku and Dabbahu Rift olivines hosting spinel inclusions have forsterite ($\text{Fo} = 100 \cdot \text{Mg}/(\text{Mg} + \text{Fe})$, in mol%) of Fo_{76-86} . There is poor correlation between olivine Fo and Al_2O_3 , especially for our Dabbahu dataset. High olivine Al_2O_3 concentrations are linked to higher T_{crys} and crystallisation from more primitive melts, therefore in the absence of Fe-Mg re-equilibration higher Fo is expected. We discuss the implications of possible Fo- Al_2O_3 decoupling in Section 3.2. Olivine Al_2O_3 does not correlate with P_2O_5 or TiO_2 , suggesting that Al_2O_3 uptake is not affected by P-Al or Ti-Al substitution (Coogan et al., 2014; Jennings et al., 2019).

The compositions of inclusions of spinel are shown in Figs. 2B and C. Fe_2O_3 is estimated from total spinel FeO on a basis of four oxygens and should be considered as approximate (Droop, 1987). All spinel inclusions fall within the calibrated Cr# and $\text{Fe}_2\text{O}_3/\text{FeO}_t$ range of the thermometer (Cr# < 0.69 and $\text{Fe}_2\text{O}_3/\text{FeO}_t$ < 0.4 respectively; Fig. 2B). Our spinels are relatively high in Ti and most samples exceed the thermometer calibration range of Ti per formula unit (p.f.u.) (< 0.025; Fig. 2C). While uptake of Ti can affect the activity coefficients of Al and Cr in spinel, biasing temperatures from high Ti spinels (e.g., Jennings et al., 2019), previous Al-exchange studies note that Ti contents < 0.32 Ti p.f.u. do not

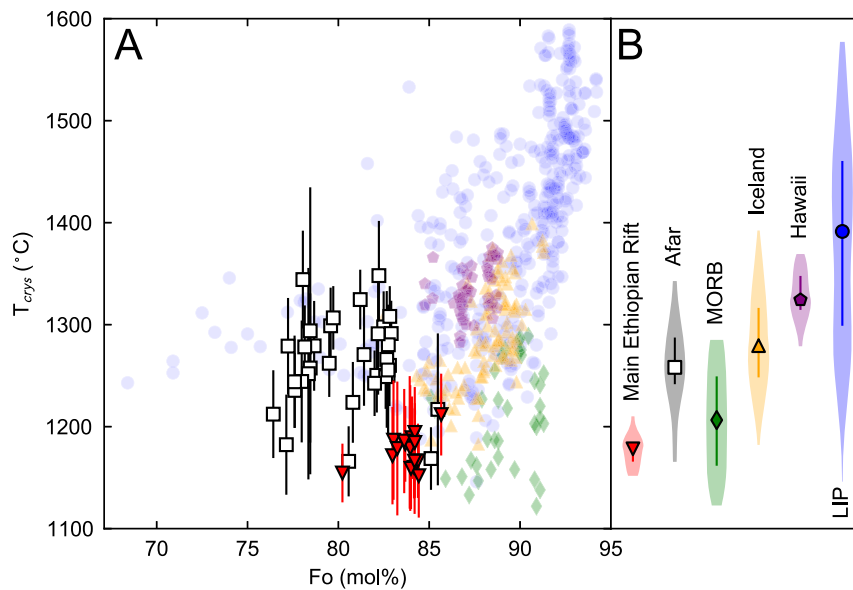


Fig. 3. Olivine crystallisation temperatures for the Main Ethiopian Rift and Afar presented alongside a global compilation of olivine-spinel Al-exchange crystallisation temperatures from different tectonic settings. A. Al-exchange crystallisation temperatures plotted against olivine Fo, with 2σ error bars. B. Violin plots of crystallisation temperatures. Markers show medians, and bars show the interquartile range. The global data has previously been compiled by Matthews et al. (2021) (see Supplementary Materials for a list of references).

produce anomalous results (Coogan et al., 2014; Heinonen et al., 2015; Jennings et al., 2019). All of the spinels used here to calculate T_{crys} values have Ti p.f.u. ≤ 0.1 (Fig. 2C).

3.2. Olivine crystallisation temperatures

Our T_{crys} results are plotted in Fig. 3. Boku T_{crys} range from $1152 \pm 40^\circ\text{C}$ to $1212 \pm 40^\circ\text{C}$ with the highest T_{crys} recorded by the most forsteritic olivine (Fo₈₆). Boku T_{crys} and Fo are well-constrained, with most T_{crys} values within mutual uncertainty and the majority of olivine-spinel pairs clustering between Fo_{82–85} and tightly between Fo_{83.5–84.5}. Dabbahu Rift olivine-spinel pairs record temperatures from $1166 \pm 34^\circ\text{C}$ to $1344 \pm 48^\circ\text{C}$, however, there is no clear trend between Fo and T_{crys} (Fig. 3), suggesting that Fo may have become decoupled from Al by diffusive exchange of Mg and Fe with the surrounding magma between crystallisation and eruption.

The mean T_{crys} of Boku olivines ($1177 \pm 16^\circ\text{C}$) is lower than that of Dabbahu ($1267 \pm 43^\circ\text{C}$). This temperature difference could imply that primary magmas at Dabbahu are hotter than Boku, assuming that the olivine captured in our sample sets are the first to crystallise. If Boku and Dabbahu magmas do crystallise at similar temperatures, it is plausible that this difference in mean T_{crys} arises from the under-sampling of crystals that fractionated earlier at Boku compared with Dabbahu.

Fig. 3 shows the T_{crys} distributions of our Ethiopian samples in comparison with those of MORB, Iceland, Hawaii, and LIPs. Boku T_{crys} are lower than the highest recorded MORB T_{crys} ($1289 \pm 34^\circ\text{C}$; Matthews et al., 2021) and record a lower median T_{crys} than that of MORB. However, Boku olivines are mostly lower Fo than the MORB olivines for which Al-exchange temperatures have been obtained. The higher temperature Dabbahu distribution overlaps with the MORB distribution as well as the plume-influenced settings of Iceland and Hawaii. Only the highest temperature Dabbahu olivines exceed the highest MORB T_{crys} , and are comparable with the highest T_{crys} recorded from Iceland and Hawaii.

The olivines used in this study are relatively evolved (lower Fo) compared to most of those which the Al-exchange thermometer has been applied previously (Fig. 3) and are unlikely to be representative of the first crystals to form from primary mantle melts,

which are typically Fo_{~91} (e.g., Rooney et al., 2005). As our melting model predicts olivine T_{crys} at the basalt liquidus, we must therefore estimate the T_{crys} of the first olivine to crystallise from the primary mantle melt ($T_{crys}^{primary}$).

Low Fo olivines can develop during fractional crystallisation or via diffusive re-equilibration with more evolved melts, for example within an interdiffusing mush pile (Thomson and MacLennan, 2013). Furthermore, pyroxenite-derived melts will crystallise lower Fo olivine than lherzolite-derived melts at the same temperatures, and progressive mixing of pyroxenite-derived melts into lherzolite-derived melts will cause the Fo content of crystallising olivine to decrease faster than in a pure lherzolite melt (see Supplementary Materials for a more detailed description). To estimate $T_{crys}^{primary}$ of the first olivine crystallising from a mantle-derived melt we must consider these mechanisms, and, if necessary, project back to higher Fo and $T_{crys}^{primary}$.

Fractional crystallisation models suggest that our Boku olivines plausibly lie on liquid line of descent from a primary basalt crystallising only olivine (Supplementary Materials Figure S4). We therefore extrapolate T_{crys} at low Fo to $T_{crys}^{primary}$ at high Fo to obtain an estimate for the liquidus temperature of the basalt. To do this we use the mean T_{crys} of the Fo_{83.5–84.5} cluster ($1175 \pm 22^\circ\text{C}$) as the starting value and the iterative olivine addition projection of Matthews et al. (2021), extrapolating to $T_{crys}^{primary}$ at Fo₉₁ (Fig. 4A); Fo₉₁ is selected for continuity with Matthews et al. (2021). This yields a $T_{crys}^{primary}$ value for Boku of $1426 \pm 26^\circ\text{C}$.

The lack of a correlation between Fo and T_{crys} in the Dabbahu Rift dataset implies that these parameters may have become decoupled since initial crystallisation of the olivines. We therefore explore three possible scenarios for obtaining a $T_{crys}^{primary}$ value from this data (Fig. 4B–D). One possibility is that these olivines have equilibrated their Fo contents with more evolved melts, in which case the highest Dabbahu T_{crys} values (mean of $1339 \pm 22^\circ\text{C}$) represent those closest to the liquidus temperature of the primary mantle melt crystallising Fo₉₁ olivine, i.e., $T_{crys} \approx T_{crys}^{primary}$ (Fig. 4B). Alternatively, if heterogeneity from unmixed lherzolite-derived and pyroxenite-derived mantle melts has not been removed by the time melts begin crystallising, then a range of Fo contents would

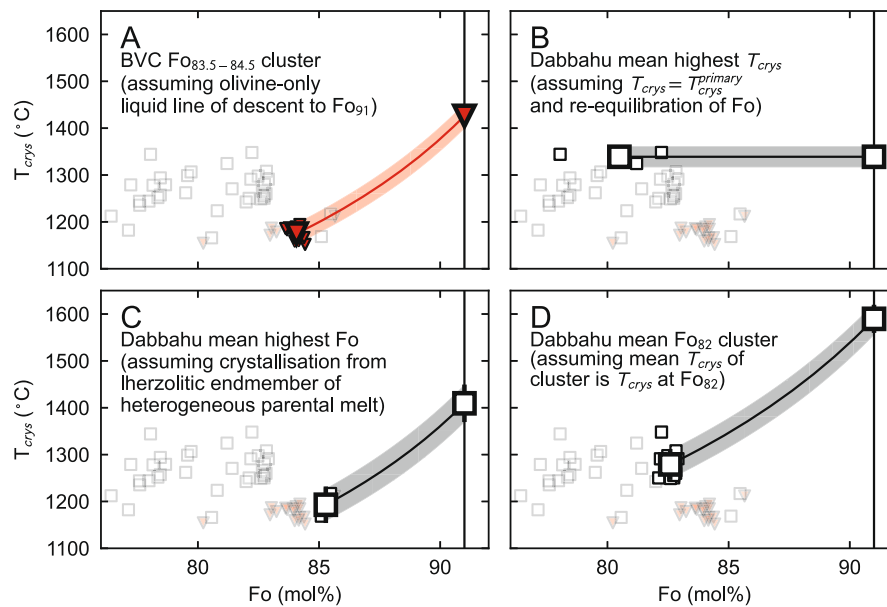


Fig. 4. Figure illustrating the iterative olivine addition used to determine primary crystallisation temperatures from temperatures obtained from our dataset. The starting temperatures are as follows: A. The mean T_{crys} of the $Fo_{83.5-84.5}$ cluster comprising the highest Fo cluster of points in our Boku dataset, projected to $T_{crys}^{primary}$ at Fo_{91} ; B. the mean of the highest Dabbahu T_{crys} values, assumed to be $T_{crys}^{primary}$; C. the mean T_{crys} of the highest Fo olivines in the Dabbahu dataset projected to $T_{crys}^{primary}$; D. the mean T_{crys} of the highest Fo cluster at Fo_{82} , projected to $T_{crys}^{primary}$. The faded triangular and square markers in the plot are the Boku and Afar T_{crys} in our dataset respectively; the small bold markers in the plots are datapoints used to calculate Fo and T_{crys} means, which are subsequently used to project to $T_{crys}^{primary}$ at Fo_{91} . The shaded area represents the propagated uncertainty of the initial crystallisation temperature estimate. In all cases the uncertainty on mean T_{crys} prior to extrapolation is the larger of the standard deviation of T_{crys} values contributing to the mean, or an uncertainty characteristic of the standard deviation of each individual value. Uncertainty in $T_{crys}^{primary}$ is determined by extrapolation of uncertainty of T_{crys} at lower Fo, and uncertainty in estimating $T_{crys}^{primary}$ is propagated by performing separate inversions for each $T_{crys}^{primary}$.

be produced at any given temperature with the highest Fo crystals forming from melts closest to the lherzolitic liquid line of descent (Matthews et al., 2021). Projecting the mean T_{crys} of the two highest Fo olivines ($1193 \pm 34^\circ\text{C}$) back along this liquid line of descent to Fo_{91} gives a $T_{crys}^{primary}$ of $1409 \pm 40^\circ\text{C}$ (Fig. 4C). A final possibility is that an initial correlation between Fo and T_{crys} , which existed due to fractional crystallisation, has been distorted by extensive re-equilibration to a common Fo value (Thomson and Maclennan, 2013). In this scenario the mean Fo of an equilibrated olivine population (in this case we use the higher Fo_{82} cluster) will still lie along the initial liquid line of descent and projecting back the mean T_{crys} should provide a reasonable estimate of $T_{crys}^{primary}$. Projecting the mean T_{crys} of the Fo_{82} cluster to Fo_{91} gives a $T_{crys}^{primary}$ of $1590 \pm 33^\circ\text{C}$ (Fig. 4D). These three estimates provide possible T_{crys} values for the Dabbahu magmas between $\sim 1339-1590^\circ\text{C}$.

3.3. Inversion results

Our inversion solutions are presented as posterior probability distributions in Figs. 5 and 6. The complete collection of parameters describing these posterior distributions are presented in Supplementary Tables S6-9, and inversion outputs are included in Supplementary Dataset S3. Figs. 5A, 6A, 6C and 6E illustrate sections through the crust and uppermost mantle, and Figs. 5B, 6B, 6D and 6F present T_p and mantle compositions. REE distributions are also illustrated in these figures (concentrations are shown inverting for ratios to illustrate the fitting between modelled and observed basalts). The absolute concentrations of model REE distributions can differ from those observed in the basalts, which can be attributed to differences in true and modelled mantle source compositions, the absence of melts not captured in our inversion model, fractional crystallisation, or a combination of these, which we consider below and in the Supplementary Materials. Selecting a mantle with lower concentrations of REEs (but the same La/Yb and

Dy/Yb ratios) will result in a REE trend that falls beneath those we model in Figs. 5 and 6.

The REE distributions resulting from our inversions are obtained by running forward models of the posterior distribution medians, which are overlain on top of sampled forward models deemed high-likelihood by the inversion algorithm for comparison. These median distributions do not reflect true solutions generated by the MULTINEST inversion or take into account co-variation between different parameters; each solution will have its own combination of parameter values. Forward model REE concentrations do not affect the calculations but are the results of them, and are ultimately controlled by the La/Yb and Dy/Yb constraints in the inversion. Also shown in Figs. 5 and 6 is the REE composition of the magma following the addition of 5% of a 1% batch lithospheric melt, before and after correction for fractional crystallisation. The addition of lithospheric melt primarily alters the concentrations of lighter REEs and can be evaluated via the effect on the fit to the observed La/Yb. As discussed below, this improves the fit between the observed and modelled magma compositions, however given the uncertainties in, and trade-offs between, the mineralogy and composition of lithospheric mantle, melt fraction, and degree of melt addition, it is not possible using our method to uniquely constrain the extent of lithospheric melting and/or contamination of the mantle-derived magmas (see Supplementary Figure S3).

3.3.1. Boku Volcanic Complex

The results of our joint T_{crys} -REE inversion for Boku are shown in Fig. 5, with $T_{crys}^{primary}$ of $1426 \pm 26^\circ\text{C}$ representing the mean T_{crys} of the $Fo_{83.5-84.5}$ cluster projected to Fo_{91} . Our inversion returns a median T_p of $1500^{+32}_{-42}^\circ\text{C}$ for a tri-lithology mantle. To match both the t_m constraint and REE concentration ratios the inversion favours a LAB depth of ~ 90 km, which falls outside the uncertainty of our prior estimate of 60 ± 20 km, suggesting that the majority of forward models trialled with this range of LAB

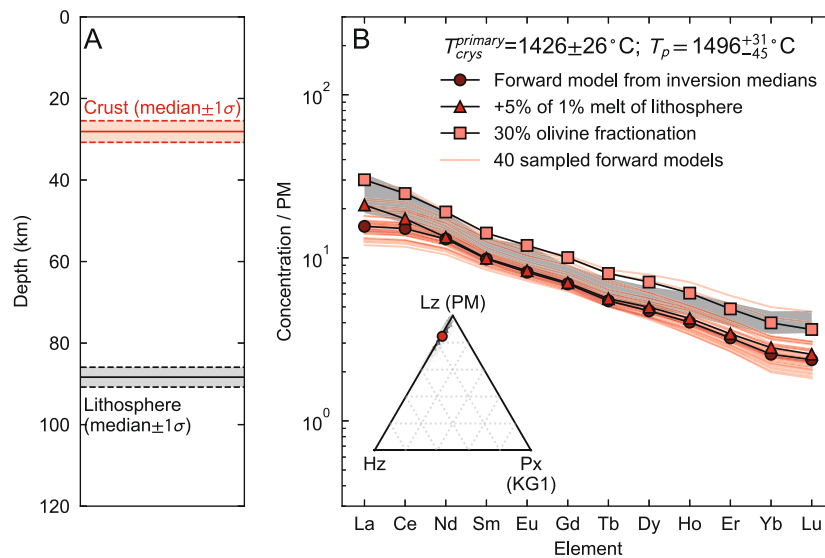


Fig. 5. Posterior distributions for mantle T_p , composition, crystallisation depth and lithospheric thickness at the Boku Volcanic Complex, Main Ethiopian Rift. The initial olivine T_{crys} of the posteriors is the mean T_{crys} of Fo_{83.5–84.5} olivines projected to T_{crys} at Fo₉₁. Subfigure A is a vertical section through the uppermost rift crust and mantle showing the most likely depths of the Moho and the lithosphere-asthenosphere boundary (LAB) as determined from our inversion. The base of the crust and lithosphere are shown as red and black lines with 1σ shaded area respectively. Subfigure B shows the REE distribution of a pyMelt forward model run using the medians of the inversion posterior distributions as starting parameters (circles), i.e., T_p (given in the subfigure legend), mantle harzburgite and pyroxenite, lithospheric thickness, and crystallisation pressure. This median forward model is overlain on 40 sampled high-likelihood forward models. The rare-earth element distribution marked with triangles is the composition of the melt upon addition of 5% small-fraction lithospheric melt, and the squares mark the same distribution upon fractionation of 30% olivine. Literature data showing basalt rare-earth element concentration ranges from Boku are illustrated as the grey area (Tadesse et al., 2019). All distributions are normalised to PM (McDonough and Sun, 1995). The inset ternary plot shows the posterior distributions of acceptable mantle compositions in a space defined by non-melting harzburgite (Hz), PM-composition lherzolite (Lz), and KG1-composition (50:50 DMM:average MORB) pyroxenite (Px). The coloured dot in the inset ternary shows the median mantle composition from which the REE distribution is derived.

depth fail to match the observed data. The median mantle resulting from our inversion is mostly PM-composition lherzolite (~80%), with the remainder predominantly harzburgite. The inversion results share La/Yb and Dy/Yb ratios within uncertainty of observed Boku basalts. The effect of introducing small-fraction lithospheric melts to our inversion result is therefore minor, but does improve the fit to the observed La/Yb. Fractionation of olivine from the primary magma sufficiently concentrates REEs in the residual melt to match observed basalts (Fig. 5).

3.3.2. Dabbahu Rift

Inversion posterior distributions for the Dabbahu Rift (Fig. 6) are derived from the three possible $T_{crys}^{primary}$ values described in Section 3.2. All Dabbahu inversions return T_p in excess of MORB (1508^{+37}_{-33} °C; 1565^{+49}_{-45} °C; 1658^{+41}_{-45} °C), in concordance with an elevated Ethiopian mantle T_p . However, the median thickness of the lithosphere in all three models is variable, with the lowest $T_{crys}^{primary}$ reproducible from a lithosphere < 50 km thick (Figs. 6A, C, E). Continued melting to shallower depths in this model (Figs. 6A and B) is required to produce sufficient volumes of magma to match the t_m constraint for Afar (13 ± 2 km) at lower T_p , whereas the other two models produce these melt volumes with significantly elevated T_p and a comparatively thicker lithosphere (Figs. 6C-F). These three model inversions illustrate a notable trade-off between T_p and LAB depth. This arises because the La/Yb constraint cannot be matched by the inversion and consequently the light REE portion of the modelled distribution deviates significantly from the observed values (Figs. 6B, D and F). Extensive melting is required to fit t_m at Afar, however this has the effect of diluting the REEs as melt generation progresses. Dy/Yb is mostly well matched by these inversions, and all three models retain the garnet signature observed in medium-heavy REEs. The addition of a minor volume of lithospheric melt significantly improves the fit to the La/Yb values (see Supplementary Materials).

The inversion with the highest starting $T_{crys}^{primary}$ of 1590 ± 33 °C returns a T_p which is ~ 300 °C hotter than ambient mantle and over 100 °C hotter than the other Dabbahu inversions (Figs. 6E and F). In contrast to the cooler models, t_m is matched by melting a highly harzburgitic mantle, which promotes substantial melting of the lherzolitic and pyroxenitic components. Of the three inversions, the REE distribution predicted from the medians of this model provides the worst fit to the observed trends (Fig. 6F). Furthermore, the best-fitting lithospheric thickness is ~ 90 km, thicker even than the lithosphere underlying the Ethiopian and Somalian plateaux (Rychert et al., 2012; Lavayssi re et al., 2018) which is highly unlikely in this mature rift system. We therefore conclude that this higher $T_{crys}^{primary}$ value is unsuitable for Dabbahu Rift magmas and the results of this inversion are not included in the following discussion.

4. Discussion

The Ethiopian mantle T_p of 1500–1550 °C suggested from the majority of our inversions are in good concordance with previous petrological and geophysical estimates (Rooney et al., 2012b; Ferguson et al., 2013b; Armitage et al., 2015). Our inversions, given the constraints placed upon them, can replicate observed T_{crys} , t_m , and medium-heavy REE distributions within this T_p range (Figs. 5 and 6). Mantle T_p also appears to be consistent within uncertainty throughout the overall Ethiopian rifting region, as the calculated T_p for the MER (1496^{+31}_{-45} °C) and Afar (1508^{+37}_{-33} °C and 1565^{+49}_{-45} °C) cannot be differentiated with confidence despite the differences in their model priors. The same conclusion is reached when considering alternative mantle compositions and active mantle upwelling (Supplementary Materials). Variability in magma generation between the northern MER and central Afar is therefore likely to be driven solely by the depth of the LAB and minor variations in source lithology.

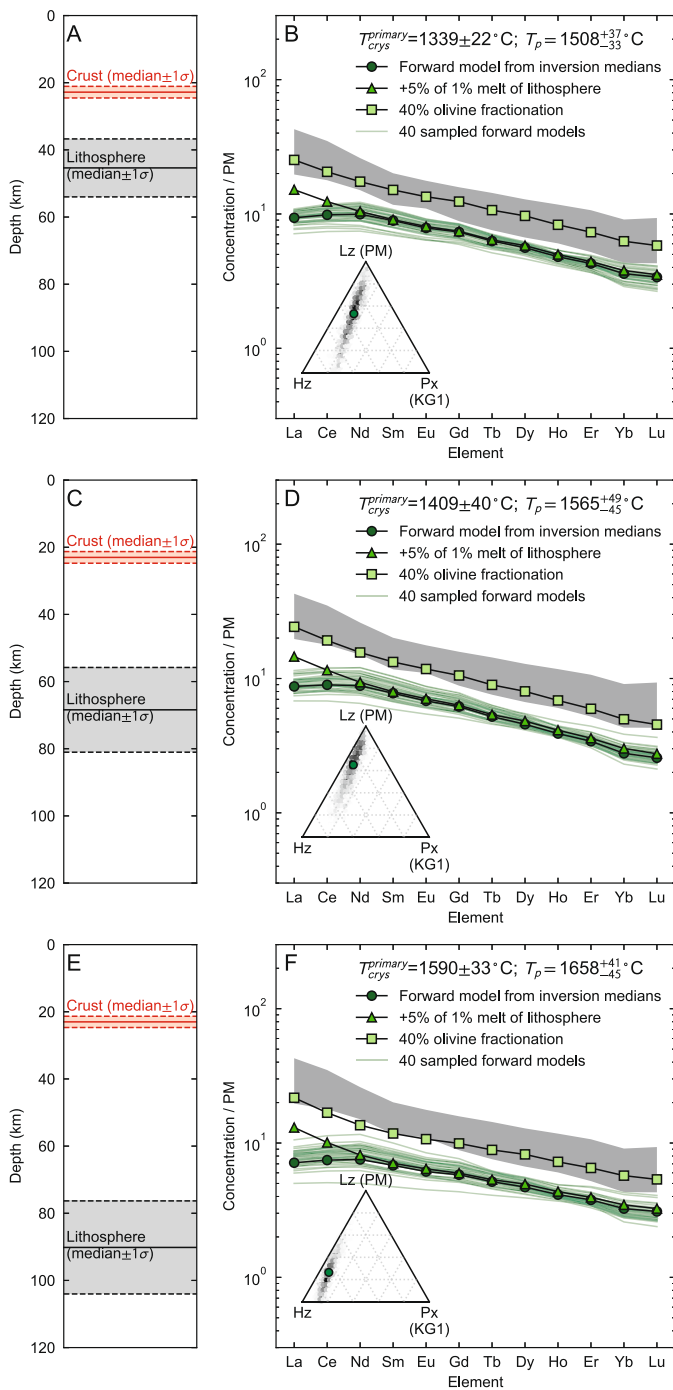


Fig. 6. Posterior distributions for mantle T_p , composition, crystallisation depth and lithospheric thickness at the Dabbahu Rift, Afar. Subfigures A and B show the results of inverting from the mean of the highest olivine T_{crys} (1339 ± 22 °C), subfigures C and D the results from projecting the T_{crys} of the highest Fo olivines to $T_{crys}^{primary}$ at Fo₉₁ (1409 ± 40 °C), subfigures E and F the results from projecting the mean T_{crys} of the highest Fo cluster (Fo₈₂) to $T_{crys}^{primary}$ at Fo₉₁ (1590 ± 33 °C). Figure contents are as described in Fig. 5. Literature data showing basalt rare-earth element concentrations are illustrated as the grey areas in subfigures B, D and F (Ferguson et al., 2013b).

The light REE data from Dabbahu, and to a lesser extent Boku, can be more closely matched with a minor addition of small-fraction lithospheric melts to our modelled mantle-derived magmas (Fig. 6, Supplementary Fig. S3). This occurs despite including La/Yb as a constraint, demonstrating that the inversion model parameters cannot combine to closely match all constraints. The involvement of lithospheric materials in the petrogenesis of these

magmas is supported by observed deficits in K versus other geochemically similar elements in magmas from the MER (Furman, 2007; Tadesse et al., 2019) and Afar (Ferguson et al., 2013b), which can arise due to interactions with K-bearing phases in metasomatised lithospheric mantle (Class and Goldstein, 1997). A detailed investigation of this process is beyond the scope of this study, but could be investigated in future work.

Our models predict that the lithological composition of the mantle under the MER is primarily a mixture of lherzolite and non-melting harzburgite (Fig. 5B), the precise proportions of which depend on the fusibility and REE composition of the melting lithologies selected for our inversions. A lower harzburgite proportion would be favoured if mantle lherzolite is more depleted in light REEs than PM, as this could allow lower degrees of lherzolite or pyroxenite melting to match observed REE distributions owing to a reduced thermal buffering effect (Supplementary Materials). Likewise, a high harzburgite proportion could result from compensating for the productivity of our chosen lherzolite and pyroxenite melting models (Matthews et al., 2016). In reality, trace element enrichment does not necessarily correlate with lithology melt productivity, as assumed in our model. In the MER, a more fusible mantle component is considered unnecessary to match REE ratios and t_m (Fig. 5B), however, such a component is required in Afar, both to introduce trace element enrichment to the melting mantle and to produce a garnet signature at depth. As a further consequence, the permitted compositional range for Afar inversions favour a mantle which is much less refractory than the MER. These mantle composition solutions form linear trends in compositional ternary space (Fig. 6B and D), which is constrained by t_m . Compositional enrichment in the mantle under Afar compared to the MER could be linked to the positioning of the Afar plume, the centre of which is considered closer to the Dabbahu Rift than Boku based on regional variations in basalt radiogenic isotope ratios (Rooney et al., 2012a).

There is a notable contrast in the predicted thickness of the lithosphere between the two localities. Our MER inversion favours a LAB depth of ~ 90 km (Fig. 5A), in general agreement with geophysical observations that mantle melting here occurs at depths > 75 km (e.g., Gallacher et al., 2016). As our Afar inversions cannot match the La/Yb constraint without the addition of lithospheric melts, a notable trade-off exists between LAB depth and T_p . Afar LAB depths are predicted to be lower than the MER (50–70 km; Figs. 6A, C, E). For the lowest $T_{crys}^{primary}$ inversion this is notably less than that estimated by Ferguson et al. (2013b) (> 80 km), who used a single lithology peridotite melting model to match observed REEs. While both our results and those of (Ferguson et al., 2013b) argue for a deep onset of melting beneath Afar due to an elevated mantle T_p , the continuation of melting to shallower depths beneath a thinner lithospheric lid predicted by our model is necessary to generate enough melt to match the central Afar t_m of 13 ± 2 km, which significantly exceeds that of the MER (4.5 ± 1.5 km). This is required even with the inclusion of a more fusible and enriched component in the mantle source, which begins melting deeper than the lherzolitic component (5–6 GPa; Fig. 7). We note that this maximum pressure of melting is also broadly consistent with Rayleigh-wave tomography (Gallacher et al., 2016). The lherzolite component begins melting at a lower pressure (3–4 GPa; Fig. 7), by which time nearly half of the available pyroxenite has melted despite the total mantle melt fraction being only $\sim 3\%$ or less (Fig. 7). In this way, the constraints on our inversion (T_{crys} , La/Yb, Dy/Yb, and t_m) can be matched by procuring the REE garnet signature at depth through extensive melting of a fusible and enriched lithology in an elevated temperature mantle before dilution of the garnet melting signature, and increasing melt volumes, via shallower melting of less productive lithologies. Further enrichment in light REEs can subsequently be achieved through minor

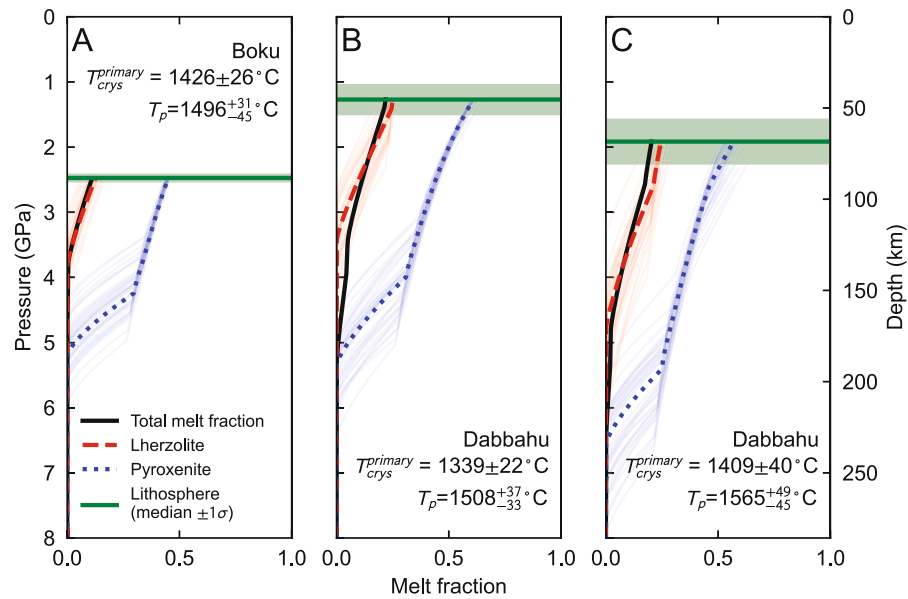


Fig. 7. Melt fraction as a function of pressure for Boku (A) and Dabbahu Rift (B and C), calculated using forward models with parameters dictated by inversion posterior distribution medians. The Afar forward models use the inversion results for the primary crystallisation temperature of $1339 \pm 22^\circ\text{C}$ (B) and $1409 \pm 40^\circ\text{C}$ (C). Melt fractions are shown for lherzolite (dashed red line), pyroxenite (dotted blue line), and the total mantle (solid black line). The solid green line and green shaded area show the position of the posterior median lithosphere with 1σ uncertainty. The faded red and blue lines represent the lherzolite and pyroxenite melting curves of 40 sampled forward models respectively.

lithospheric melting. < 70 km LAB depths are not necessarily unexpected for Afar as geophysical models have returned similar values (Armitage et al., 2015). The difference in lithospheric thickness between the MER and central Afar is consistent with the latter being at a more-evolved stage of rifting. However, as proposed by Bastow and Keir (2011) and Ferguson et al. (2013b), significant lithospheric thinning still appears to be necessary at the Dabbahu Rift before plate rupture and the onset of true oceanic spreading.

Fig. 8 compares the T_p values from our inversions to T_p from other locations that have been determined using the same approach and melting models (Matthews et al., 2021). The median T_p of the Ethiopian mantle is hotter than the Siqueiros MORB-source mantle ($1364 \pm 23^\circ\text{C}$), and overlaps with the T_p posterior distributions of other plume-influenced settings such as Iceland and Hawaii. The Ethiopian mantle under Afar is also expected to have a greater proportion of a more enriched melting lithological component than the MORB-source mantle, similar perhaps to that of Iceland (Matthews et al., 2016, 2021). To constrain this further, future work on primitive Ethiopian basalts, melt inclusions, or xenoliths will be necessary to identify compositional variations in parental basalts attributable to a lithologically heterogeneous source mantle (e.g., Shorttle et al., 2014). Likewise, new information on the storage conditions of olivines at the Dabbahu rift will contribute to a better estimate of $T_{crys}^{primary}$, which will enable better constrained estimates of mantle T_p .

5. Conclusions

Previous geophysical observations of the MER and Afar mantle suggest that mantle temperatures are elevated, and melting in the rift occurs at depth. Through olivine-spinel Al-exchange thermometry we obtain new petrological olivine crystallisation temperatures for the MER and Afar, with means of $1176 \pm 16^\circ\text{C}$ and $1263 \pm 43^\circ\text{C}$ respectively. Extrapolation of T_{crys} from low Fo olivines to $T_{crys}^{primary}$ at which olivines in equilibrium with mantle-derived melts are likely to crystallise, when combined with a model of mantle melting and observed basalt REE concentrations, forms the basis for inversion of mantle temperature and lithology. Our mod-

els reproduce observed crystallisation temperatures and REE concentrations with elevated mantle temperatures that are consistent across Ethiopia ($1496^{+31}_{-45}^\circ\text{C}$ at Boku; $1508^{+37}_{-33}^\circ\text{C}$ and $1565^{+49}_{-45}^\circ\text{C}$ at Afar depending on $T_{crys}^{primary}$).

The primary differences between the two rift locations are lithospheric thickness and possibly mantle composition. Lithospheric thickness is estimated to be ~ 90 km at the MER but ≤ 70 km at Afar. The primary observed consequence of this lithospheric thinning is the thicknesses of intruded melt present at these two locations, and can be attributed to a more evolved rift system in Afar. Compositionally, the MER mantle is predicted to contain a lower fraction of more enriched lithologies than the Afar mantle (Figs. 5 and 6). Garnet signatures observed in REE distributions from rift basalts from both these localities are expected to be influenced by melting of enriched lithologies at depth, with small-fraction lithospheric melts possibly contributing to light REE concentrations as asthenospheric melts leave the convecting mantle. The presence of enriched asthenospheric lithologies can possibly be attributed to the positioning of a large-scale plume centred on Afar (Rooney et al., 2012a). This compositional difference also contributes to the differences in melt thickness between the two locations. Our results demonstrate that, while elevated relative to mid-ocean ridges, there are no significant mantle temperature variations across the rifting Ethiopian mantle and that variability in rift-related melt generation between the northern MER and in central Afar can be attributed to differences in mantle composition and rift geodynamics.

CRedit authorship contribution statement

Kevin Wong: Project design, Field sample collection, Data collection, Modelling and coding, Data analysis and interpretation, Manuscript writing. **David Ferguson:** Project design, Project supervision, Field sample collection, Modelling and coding, Data analysis and interpretation, Manuscript writing. **Simon Matthews:** Modelling and coding, Data analysis and interpretation, Manuscript writing. **Daniel Morgan:** Project design, Project supervision, Data analysis and interpretation. **Amdemichael Zafu Tadesse:** Field sam-

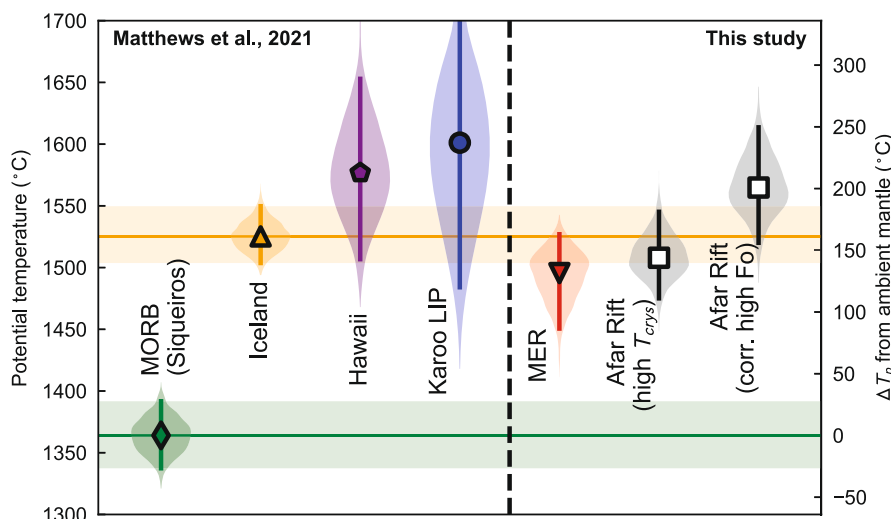


Fig. 8. Violin plots of potential temperature determined through inversion of pyMelt. The Afar temperature distributions are the inversion results for primary crystallisation temperature of $1339 \pm 22^\circ\text{C}$ and $1409 \pm 40^\circ\text{C}$. Bars within violin plots show 95% confidence interval, and markers display medians. Potential temperature posterior distributions for MORB, Iceland, Hawaii and the Karoo LIP are inversion results from Matthews et al. (2021).

ple collection, Manuscript writing. **Yared Sinetebeb:** Field sample collection. **Gezahegn Yirgu:** Project design, Project supervision, Field sample collection.

Declaration of competing interest

The authors declare that they have no known competing financial interests or personal relationships that could have appeared to influence the work reported in this paper.

Data availability

The analytical data generated by this study are available in Datasets S1 S2, and S3, which is archived in a Zenodo repository with DOI <https://doi.org/10.5281/zenodo.6786908>. PyMelt and the inversion code used in this study are archived in Zenodo repositories with <https://doi.org/10.5281/zenodo.6013925> and <https://doi.org/10.5281/zenodo.6786875> respectively.

Acknowledgements

This work was supported by a NERC PhD studentship (NE/L002574/1) awarded to KW. We thank Richard Walshaw for assistance with the electron probe analyses, and express our gratitude to the Oromia state administration and the Ethiopian Ministry of Mines and Petroleum for field and sample shipment permissions respectively. We are grateful also for constructive comments provided by the Editor (R. Hickey-Vargas) and the two anonymous reviewers that greatly improved the quality of this manuscript.

Appendix A. Supplementary material

Supplementary material related to this article can be found online at <https://doi.org/10.1016/j.epsl.2022.117820>.

References

Armitage, J.J., Ferguson, D.J., Goes, S., Hammond, J.O.S., Calais, E., Rychert, C.A., Harmon, N., 2015. Upper mantle temperature and the onset of extension and break-up in Afar, Africa. *Earth Planet. Sci. Lett.* 418, 78–90. <https://doi.org/10.1016/j.epsl.2015.02.039>. <http://www.sciencedirect.com/science/article/pii/S0012821X15001259>.

Bastow, I.D., Keir, D., 2011. The protracted development of the continent–ocean transition in Afar. *Nat. Geosci.* 4, 248–250. <https://doi.org/10.1038/ngeo1095>. <https://www.nature.com/articles/ngeo1095>.

Bastow, I.D., Nyblade, A.A., Stuart, G.W., Rooney, T.O., Benoit, M.H., 2008. Upper mantle seismic structure beneath the Ethiopian hot spot: Rifting at the edge of the African low-velocity anomaly. *Geochem. Geophys. Geosyst.* 9. <https://doi.org/10.1029/2008GC002107>. URL: <https://agupubs.onlinelibrary.wiley.com/doi/full/10.1029/2008GC002107>.

Buchner, J., Georgakakis, A., Nandra, K., Hsu, L., Rangel, C., Brightman, M., Merloni, A., Salvato, M., Donley, J., Kocovski, D., 2014. X-ray spectral modelling of the AGN obscuring region in the CDFS: Bayesian model selection and catalogue. *Astron. Astrophys.* 564, A125. <https://doi.org/10.1051/0004-6361/201322971>. <https://www.aanda.org/articles/aa/abs/2014/04/aa22971-13/aa22971-13.html>. publisher: EDP Sciences.

Casagli, A., Frezzotti, M.L., Peccerillo, A., Tiepolo, M., De Astis, G., 2017. (Garnet)-spinel peridotite xenoliths from Mega (Ethiopia): evidence for rejuvenation and dynamic thinning of the lithosphere beneath the southern Main Ethiopian Rift. *Chem. Geol.* 455, 231–248. <https://doi.org/10.1016/j.chemgeo.2016.11.001>. <http://www.sciencedirect.com/science/article/pii/S0009254116305940>.

Class, C., Goldstein, S.L., 1997. Plume-lithosphere interactions in the ocean basins: constraints from the source mineralogy. *Earth Planet. Sci. Lett.* 150, 245–260. [https://doi.org/10.1016/S0012-821X\(97\)00089-7](https://doi.org/10.1016/S0012-821X(97)00089-7). <https://linkinghub.elsevier.com/retrieve/pii/S0012821X97000897>.

Coogan, L.A., Saunders, A.D., Wilson, R.N., 2014. Aluminum-in-olivine thermometry of primitive basalts: evidence of an anomalously hot mantle source for large igneous provinces. *Chem. Geol.* 368, 1–10. <https://doi.org/10.1016/j.chemgeo.2014.01.004>. <http://www.sciencedirect.com/science/article/pii/S0009254114000278>.

Desissa, M., Johnson, N.E., Whaler, K.A., Hautot, S., Fisseha, S., Dawes, G.J.K., 2013. A mantle magma reservoir beneath an incipient mid-ocean ridge in Afar, Ethiopia. *Nat. Geosci.* 6, 861–865. <https://doi.org/10.1038/ngeo1925>. <http://www.nature.com/ngeo/journal/v6/n10/abs/ngeo1925.html>.

Droop, G.T.R., 1987. A general equation for estimating Fe³⁺ concentrations in ferromagnesian silicates and oxides from microprobe analyses, using stoichiometric criteria. *Mineral. Mag.* 51, 431–435. <https://doi.org/10.1180/minmag.1987.051.361.10>.

Ferguson, D.J., Barne, T.D., Pyle, D.M., Oppenheimer, C., Yirgu, G., Lewi, E., Kidane, T., Carn, S., Hamling, I., 2010. Recent rift-related volcanism in Afar, Ethiopia. *Earth Planet. Sci. Lett.* 292, 409–418. <https://doi.org/10.1016/j.epsl.2010.02.010>. <http://www.sciencedirect.com/science/article/pii/S0012821X10001123>.

Ferguson, D.J., Calvert, A.T., Pyle, D.M., Blundy, J.D., Yirgu, G., Wright, T.J., 2013a. Constraining timescales of focused magmatic accretion and extension in the Afar crust using lava geochronology. *Nat. Commun.* 4, 1416. <https://doi.org/10.1038/ncomms2410>. <https://www.nature.com/articles/ncomms2410>.

Ferguson, D.J., MacLennan, J., Bastow, I.D., Pyle, D.M., Jones, S.M., Keir, D., Blundy, J.D., Plank, T., Yirgu, G., 2013b. Melting during late-stage rifting in Afar is hot and deep. *Nature* 499, 70–73. <https://doi.org/10.1038/nature12292>. <https://www.nature.com/articles/nature12292>.

Feroz, F., Hobson, M.P., Cameron, E., Pettitt, A.N., 2019. Importance nested sampling and the MultiNest algorithm. *Open J. Astrophys.* 2. <https://doi.org/10.21105/astro.1306.2144>.

Field, L., Blundy, J., Calvert, A., Yirgu, G., 2013. Magmatic history of Dabbahu, a composite volcano in the Afar Rift, Ethiopia. *Geol. Soc. Am. Bull.* 125, 128–147. <https://doi.org/10.1130/B30560.1>. <https://pubs.geoscienceworld.org/gsabulletin/article/125/1-2/128-147/125828>.

- Furman, T., 2007. Geochemistry of East African Rift basalts: an overview. *J. Afr. Earth Sci.* 48, 147–160. <https://doi.org/10.1016/j.jafrearsci.2006.06.009>. <http://www.sciencedirect.com/science/article/pii/S1464343X07000271>.
- Furman, T., Nelson, W.R., Elkins-Tanton, L.T., 2016. Evolution of the East African rift: drip magmatism, lithospheric thinning and mafic volcanism. *Geochim. Cosmochim. Acta* 185, 418–434. <https://doi.org/10.1016/j.gca.2016.03.024>. <http://www.sciencedirect.com/science/article/pii/S0016703716301338>.
- Gale, A., Dalton, C.A., Langmuir, C.H., Su, Y., Schilling, J.G., 2013. The mean composition of ocean ridge basalts. *Geochim. Geophys. Geosyst.* 14, 489–518. <https://doi.org/10.1029/2012GC004334>. <https://agupubs.onlinelibrary.wiley.com/doi/full/10.1029/2012GC004334>.
- Gallacher, R.J., Keir, D., Harmon, N., Stuart, G., Leroy, S., Hammond, J.O.S., Kendall, J.M., Ayele, A., Goitom, B., Ogubazghi, G., Ahmed, A., 2016. The initiation of segmented buoyancy-driven melting during continental breakup. *Nat. Commun.* 7, 13110. <https://doi.org/10.1038/ncomms13110>. <http://www.nature.com/doi/10.1038/ncomms13110>.
- Hammond, J.O.S., Kendall, J.M., Stuart, G., Ebinger, C., Bastow, I., Keir, D., Ayele, A., Belachew, M., Goitom, B., Ogubazghi, G., Wright, T., 2013. Mantle upwelling and initiation of rift segmentation beneath the Afar Depression. *Geology* 41, 635–638. <https://doi.org/10.1130/G33925.1>. <http://pubs.geoscienceworld.org/geology/article/41/6/635/131210/Mantle-upwelling-and-initiation-of-rift>.
- Hammond, J.O.S., Kendall, J.M., Stuart, G.W., Keir, D., Ebinger, C., Ayele, A., Belachew, M., 2011. The nature of the crust beneath the Afar triple junction: evidence from receiver functions. *Geochim. Geophys. Geosyst.* 12. <https://doi.org/10.1029/2011GC003738>. <https://agupubs.onlinelibrary.wiley.com/doi/abs/10.1029/2011GC003738>. <https://agupubs.onlinelibrary.wiley.com/doi/pdf/10.1029/2011GC003738>.
- Hayward, N.J., Ebinger, C.J., 1996. Variations in the along-axis segmentation of the Afar Rift system. *Tectonics* 15, 244–257. <https://doi.org/10.1029/95TC02292>. <https://agupubs.onlinelibrary.wiley.com/doi/abs/10.1029/95TC02292>.
- Heinonen, J.S., Jennings, E.S., Riley, T.R., 2015. Crystallisation temperatures of the most Mg-rich magmas of the Karoo LIP on the basis of Al-in-olivine thermometry. *Chem. Geol.* 411, 26–35. <https://doi.org/10.1016/j.chemgeo.2015.06.015>. <http://www.sciencedirect.com/science/article/pii/S0009254115003034>.
- Herzberg, C., 2011. Identification of source lithology in the Hawaiian and Canary Islands: implications for origins. *J. Petrol.* 52, 113–146. <https://doi.org/10.1093/petrology/egq075>. <https://academic.oup.com/petrology/article/52/1/113/1443238>.
- Hofmann, C., Courtillot, V., Féraud, G., Rochette, P., Yirgu, G., Ketefo, E., Pik, R., 1997. Timing of the Ethiopian flood basalt event and implications for plume birth and global change. *Nature* 389, 838–841. <https://doi.org/10.1038/39853>. <https://www.nature.com/articles/39853>.
- Iddon, F., Edmonds, M., 2020. Volatile-rich magmas distributed through the upper crust in the main Ethiopian rift. *Geochim. Geophys. Geosyst.* 21, e2019GC008904. <https://doi.org/10.1029/2019GC008904>. <https://agupubs.onlinelibrary.wiley.com/doi/abs/10.1029/2019GC008904>. <https://agupubs.onlinelibrary.wiley.com/doi/pdf/10.1029/2019GC008904>.
- Jennings, E.S., Gibson, S.A., MacLennan, J., 2019. Hot primary melts and mantle source for the Paraná-Etendeka flood basalt province: new constraints from Al-in-olivine thermometry. *Chem. Geol.* 529, 119287. <https://doi.org/10.1016/j.chemgeo.2019.119287>. <http://www.sciencedirect.com/science/article/pii/S0009254119303948>.
- Kogiso, T., Hirose, K., Takahashi, E., 1998. Melting experiments on homogeneous mixtures of peridotite and basalt: application to the genesis of ocean island basalts. *Earth Planet. Sci. Lett.* 162, 45–61. [https://doi.org/10.1016/S0012-821X\(98\)00156-3](https://doi.org/10.1016/S0012-821X(98)00156-3). <http://www.sciencedirect.com/science/article/pii/S0012821X98001563>.
- Lavayssière, A., Rychert, C., Harmon, N., Keir, D., Hammond, J.O.S., Kendall, J.M., Doubré, C., Leroy, S., 2018. Imaging lithospheric discontinuities beneath the northern East African rift using s-to-p receiver functions. *Geochim. Geophys. Geosyst.* <https://doi.org/10.1029/2018GC007463>. <https://agupubs.onlinelibrary.wiley.com/doi/abs/10.1029/2018GC007463>.
- Maguire, P., Keller, G., Klemperer, S., Mackenzie, G., Keranen, K., Harder, S., O'Reilly, B., Thybo, H., Asfaw, L., Khan, M., Amha, M., 2006. Crustal structure of the northern Main Ethiopian Rift from the EAGLE controlled-source survey; a snapshot of incipient lithospheric break-up. In: *The Afar Volcanic Province Within the East African Rift System*. In: Geological Society London Special Publications, vol. 259, pp. 269–292. <http://sp.lyellcollection.org/lookup/doi/10.1144/GSL.SP.2006.259.01.21>.
- Matthews, S., Shorttle, O., MacLennan, J., 2016. The temperature of the Icelandic mantle from olivine-spinel aluminum exchange thermometry. *Geochim. Geophys. Geosyst.* 17, 4725–4752. <https://doi.org/10.1002/2016GC006497>. <http://onlinelibrary.wiley.com/doi/10.1002/2016GC006497/abstract>.
- Matthews, S., Wong, K., Gleeson, M.L.M., 2022. PyMelt: an extensible python engine for mantle melting calculations. <https://eartharxiv.org/repository/view/3101/>. publisher: EarthArXiv.
- Matthews, S., Wong, K., Shorttle, O., Edmonds, M., MacLennan, J., 2021. Do olivine crystallization temperatures faithfully record mantle temperature variability? *Geochim. Geophys. Geosyst.* <https://doi.org/10.1029/2020GC009157>. <https://onlinelibrary.wiley.com/doi/10.1029/2020GC009157>.
- McDonough, W.F., Sun, S.S., 1995. The composition of the Earth. *Chem. Geol.* 120, 223–253. [https://doi.org/10.1016/0009-2541\(94\)00140-4](https://doi.org/10.1016/0009-2541(94)00140-4).
- McKenzie, D., O'Nions, R.K., 1991. Partial melt distributions from inversion of rare Earth element concentrations. *J. Petrol.* 32, 1021–1091. <https://doi.org/10.1093/petrology/32.5.1021>. <https://academic.oup.com/petrology/article/32/5/1021/1499015>.
- Phipps Morgan, J., 2001. Thermodynamics of pressure release melting of a veined plum pudding mantle. *Geochim. Geophys. Geosyst.* 2, 1001. <https://doi.org/10.1029/2000GC000049>. <http://onlinelibrary.wiley.com/doi/10.1029/2000GC000049/abstract>.
- Plank, T., Langmuir, C.H., 1992. Effects of the melting regime on the composition of the oceanic crust. *J. Geophys. Res., Solid Earth* 97, 19749–19770. <https://doi.org/10.1029/92JB01769>. <https://agupubs.onlinelibrary.wiley.com/doi/abs/10.1029/92JB01769>. <https://agupubs.onlinelibrary.wiley.com/doi/pdf/10.1029/92JB01769>.
- Rooney, T.O., Bastow, I.D., Keir, D., 2011. Insights into extensional processes during magma assisted rifting: evidence from aligned scoria cones. *J. Volcanol. Geotherm. Res.* 201, 83–96. <https://doi.org/10.1016/j.jvolgeores.2010.07.019>. <http://www.sciencedirect.com/science/article/pii/S0377027310002386>.
- Rooney, T.O., Furman, T., Yirgu, G., Ayalew, D., 2005. Structure of the Ethiopian lithosphere: xenolith evidence in the Main Ethiopian Rift. *Geochim. Cosmochim. Acta* 69, 3889–3910. <https://doi.org/10.1016/j.gca.2005.03.043>. <http://www.sciencedirect.com/science/article/pii/S0016703705003042>.
- Rooney, T.O., Hanan, B.B., Graham, D.W., Furman, T., Blichert-Toft, J., Schilling, J.G., 2012a. Upper mantle pollution during afar plume–continental rift interaction. *J. Petrol.* 53, 365–389. <https://doi.org/10.1093/petrology/egr065>. <https://academic.oup.com/petrology/article/53/2/365/1537319>.
- Rooney, T.O., Herzberg, C., Bastow, I.D., 2012b. Elevated mantle temperature beneath East Africa. *Geology* 40, 27–30. <https://doi.org/10.1130/G32382.1>. <https://pubs.geoscienceworld.org/gsa/geology/article-abstract/40/1/27/130670/elevated-mantle-temperature-beneath-east-africa>.
- Rooney, T.O., Nelson, W.R., Ayalew, D., Hanan, B., Yirgu, G., Kappelman, J., 2017. Melting the lithosphere: metasomes as a source for mantle-derived magmas. *Earth Planet. Sci. Lett.* 461, 105–118. <https://doi.org/10.1016/j.epsl.2016.12.010>. <http://www.sciencedirect.com/science/article/pii/S0012821X16307105>.
- Rychert, C.A., Hammond, J.O.S., Harmon, N., Michael Kendall, J., Keir, D., Ebinger, C., Bastow, I.D., Ayele, A., Belachew, M., Stuart, G., 2012. Volcanism in the Afar Rift sustained by decompression melting with minimal plume influence. *Nat. Geosci.* 5, 406–409. <https://doi.org/10.1038/ngeo1455>. <https://www.nature.com/articles/ngeo1455>.
- Shorttle, O., MacLennan, J., Lambart, S., 2014. Quantifying lithological variability in the mantle. *Earth Planet. Sci. Lett.* 395, 24–40. <https://doi.org/10.1016/j.epsl.2014.03.040>. <http://www.sciencedirect.com/science/article/pii/S0012821X14001927>.
- Spandler, C., O'Neill, H.S.C., 2010. Diffusion and partition coefficients of minor and trace elements in San Carlos olivine at 1,300 °C with some geochemical implications. *Contrib. Mineral. Petrol.* 159, 791–818. <https://doi.org/10.1007/s00410-009-0456-8>. <https://link.springer.com/article/10.1007/s00410-009-0456-8>.
- Stracke, A., Genske, F., Berndt, J., Koornneef, J.M., 2019. Ubiquitous ultra-depleted domains in Earth's mantle. *Nature Geoscience* 12 (10), 851–855. <https://doi.org/10.1038/s41561-019-0446-z>. <https://www.nature.com/articles/s41561-019-0446-z>. Publisher: Nature Publishing Group.
- Tadesse, A.Z., Ayalew, D., Pik, R., Yirgu, G., Fontijn, K., 2019. Magmatic evolution of the Boku Volcanic Complex, Main Ethiopian Rift. *J. Afr. Earth Sci.* 149, 109–130. <https://doi.org/10.1016/j.jafrearsci.2018.08.003>. <http://www.sciencedirect.com/science/article/pii/S1464343X18302450>.
- Takahashi, E., 1986. Melting of a dry peridotite KLB-1 up to 14 GPa: implications on the origin of peridotitic upper mantle. *J. Geophys. Res., Solid Earth* 91, 9367–9382. <https://doi.org/10.1029/JB091iB09p09367>. <https://agupubs.onlinelibrary.wiley.com/doi/abs/10.1029/JB091iB09p09367>.
- Thomson, A., MacLennan, J., 2013. The distribution of olivine compositions in Icelandic basalts and picrites. *J. Petrol.* 54, 745–768. <https://doi.org/10.1093/petrology/egs083>. <https://academic.oup.com/petrology/article/54/4/745/1548250>.
- Wan, Z., Coogan, L.A., Canil, D., 2008. Experimental calibration of aluminum partitioning between olivine and spinel as a geothermometer. *Am. Mineral.* 93, 1142–1147. <https://doi.org/10.2138/am.2008.2758>. <https://pubs.geoscienceworld.org/ammin/article/93/7/1142-1147/44773>.
- Workman, R.K., Hart, S.R., 2005. Major and trace element composition of the depleted MORB mantle (DMM). *Earth Planet. Sci. Lett.* 231, 53–72. <https://doi.org/10.1016/j.epsl.2004.12.005>. <https://linkinghub.elsevier.com/retrieve/pii/S0012821X040007101>.